Hydrogen bond blueshifts in nitrile vibrational spectra are dictated by hydrogen bond geometry and dynamics

Jacob M. Kirsh[a] & Jacek Kozuch[b,c,*]

[a] Department of Chemistry, Stanford University, Stanford, California 94305-5012, United States; orcid.org/0000-0002-1444-2913
[b] Freie Universität Berlin, Physics Department, Experimental Molecular Biophysics, Arnimallee 14, 14195, Germany; https://orcid.org/0000-0002-2115-4899
[c] Freie Universität Berlin, SupraFAB Research Building, Altensteinstr. 23a, 14195 Berlin, Germany
*email: jacek.kozuch@fu-berlin.de

ABSTRACT: Vibrational Stark effect (VSE) spectroscopy has become one of the most important experimental approaches to determine the strength of noncovalent, electrostatic interactions in chemistry and biology and to quantify their influence on structure and reactivity. Nitriles (C≡N) have been widely used as VSE probes, but their application has been complicated by an anomalous hydrogen bond (HB) blueshift which is not encompassed within the VSE framework. We present an empirical model describing the anomalous HB blueshift in terms of H-bonding geometry, i.e. as a function of HB distance and angle with respect to the C≡N group. This model is obtained by comparing vibrational observables from density functional theory and electrostatics from the polarizable AMOEBA force field, and it provides a physical explanation for the HB blueshift in terms of underlying multipolar and Pauli repulsion contributions. Additionally, we compare predicted blueshifts with experimental results and find our model provides a useful, direct framework to analyze HB geometry for rigid HBs, such as within proteins or chemical frameworks. In contrast, nitriles in highly dynamic H-bonding environments like protic solvents are no longer a function solely of geometry; this is a consequence of motional narrowing, which we demonstrate by simulating IR spectra. Overall, when HB geometry and dynamics are accounted for, an excellent correlation is found between observed and predicted HB blueshifts. This correlation includes different types of nitriles and HB donors, suggesting that our model is general and can aid in understanding HB blueshifts wherever nitriles can be implemented.

INTRODUCTION

Hydrogen bonds (HBs) are among the most important noncovalent interactions in chemistry and biology.[1,2] For instance, they play a key structural role in the (self-)assembly of supramolecular complexes[3,4] and the folding of DNA, peptides, and proteins.[5–7] Furthermore, HBs often act as essential motifs to accelerate reactions in both organocatalytic[8–10] and enzymatic settings.[11–13] Despite their importance, relatively few experimental methods exist that can be used to characterize HBs within a quantitative, physical framework. One such method is vibrational Stark effect (VSE) spectroscopy, which enables the measurement of local electric field strengths of specific noncovalent interactions via changes to observables in vibrational spectra.[14] As such, VSE spectroscopy has been used to measure electric fields in solvents,[15–17] at electrode interfaces,[18–22] and in membranes[23–25] and proteins.[26–30] The VSE describes the influence of an electric field ($\vec{F}$) on a vibrational frequency ($\bar{\nu}$; in units of cm^{-1}) via the dipolar VSE equation

$$\bar{\nu}(\vec{F}) = \bar{\nu}_0 - \Delta\vec{\mu}\cdot\vec{F} - \frac{1}{2}\vec{F}\cdot\Delta\underline{\alpha}\cdot\vec{F} \quad (1a)$$

with the zero-field frequency $\bar{\nu}_0$, the difference dipole $\Delta\vec{\mu}$, (i.e. the linear field sensitivity with its magnitude $|\Delta\vec{\mu}|$ referred to as the Stark tuning rate), and the difference polarizability $\Delta\underline{\alpha}$.[14] Further, eq. 1a is often written in linear form

$$\bar{\nu}(\vec{F}) = \bar{\nu}_0 - \Delta\vec{\mu}\cdot\vec{F} \quad (1b)$$

because $\Delta\underline{\alpha}$ is typically experimentally negligible.[14] Several vibrational modes, such as the carbonyl (C=O) stretch,[14,27,29,31–33] have become very useful VSE sensors because they behave according to eq. 1b.[14,34] As such, they have enabled the assessment of electric field strengths for HBs and other noncovalent interactions in the condensed phase.[15,16,32,35,36]

The nitrile (C≡N) stretch is the most commonly used vibrational probe,[14,37–44] since it appears in an uncluttered region of the infrared (IR) spectrum and because nitriles are easily introduced into biological environments like proteins (via drugs or noncanonical amino acids)[39,45,46] or chemical settings like surfaces.[19,20,47] Despite its popularity, C≡N frequency tuning can exhibit complicated behavior that does not always follow the VSE (Fig. 1A). In aprotic environments, the C≡N stretch shows a linear $\bar{\nu}/\vec{F}$-behavior as described by eq. 1b. However, in H-bonding environments, anomalous frequency shifts are observed which are inconsistent with eq. 1b.[18,19,38,48–50] Further, this anomalous behavior cannot be explained by relevant quadratic electric field contributions due to $\Delta\underline{\alpha}$, that is, eq. 1a also cannot describe the frequency tuning.[50–52] Instead, a description of nitrile frequencies requires the introduction of an additional variable called the HB blueshift $\Delta\bar{\nu}_{HB}$,[48,53,54] to account for 'C≡N···H' interactions:

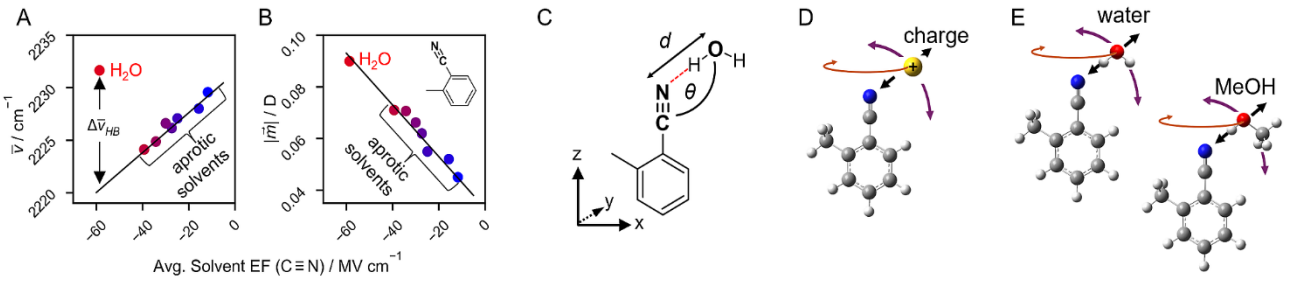

Figure 1: The C≡N stretch transition dipole $|\vec{m}|$ is a linear electric field probe, in contrast to the vibrational frequency $\bar{\nu}$, which is complicated by the HB blueshift $\Delta\bar{\nu}_{HB}$. (A) The experimental $\bar{\nu}$ of the C≡N stretch of oTN (*o*-tolunitrile, see inset in B) shows a linear trend with electric field that can be modelled with the linear VSE eq. 1b (black line) only for aprotic solvents. In water, a deviation from the line is observed, indicating C≡N frequencies require an additional term, $\Delta\bar{\nu}_{HB}$, to account for H-bonding interactions (eq. 2). (B) In contrast, $|\vec{m}|$ increases linearly with electric fields in aprotic solvents *and* water, as modelled with the VSE (eq. 3a; black line). (C) We model $\Delta\bar{\nu}_{HB}$ in terms of the heavy atom HB distance d(C≡N---$O_{HB\text{-}donor}$) and the HB angle θ(C≡N---$O_{HB\text{-}donor}$), d and θ, respectively. (D, E) To derive this model, density functional theory (DFT) calculations were performed to obtain nitrile frequencies and TDMs for oTN in two types of environments: (D) purely electrostatic environments where the nitrile interacts with a positive point charge and (E) H-bonding environments where the nitrile interacts with a water or methanol (MeOH) molecule; in all cases, the distance (black arrows) and angle (violet and orange arrows) of the interacting particle was varied. A and B are reproduced with permission from ref. [50]. Copyright 2022 American Chemical Society.

$$\bar{\nu}\left(\vec{F}, \Delta\bar{\nu}_{HB}\right) = \bar{\nu}\left(\vec{F}\right) + \Delta\bar{\nu}_{HB}. \quad (2)$$

where $\bar{\nu}\left(\vec{F}\right)$ is defined in eq. 1a/b.

Various approaches have attempted to indirectly correct for this anomaly in the nitrile's $\bar{\nu}/\vec{F}$-behavior in H-bonding environments via temperature-dependent experiments,[54] correlations with nuclear magnetic resonance,[48] or molecular dynamics (MD).[40] Recently, we found a new, direct approach to circumvent the issues with nitrile frequencies when we observed that the integrated IR absorption intensity (I_{IR}) of nitriles varies monotonically with the electric field in both aprotic and protic solvents (Fig. 1B).[50] This additional VSE is explained by the dependence of the transition dipole moment (TDM; $\vec{m}$), which governs the IR absorbance, with the electric field according to

$$\vec{m}\left(\vec{F}\right) = \vec{m}_0 - \underline{A} \cdot \vec{F} \quad (3a)$$

with

$$\sqrt{I_{IR}} \propto \left|\vec{m}\left(\vec{F}\right)\right| \quad (3b)$$

where $\vec{m}_0$ and $\underline{A}$ are the zero-field transition dipole and the transition dipole polarizability, respectively.[50] Importantly, measuring nitrile TDMs enables quantification of nitrile electric fields in H-bonding environments by using eq. 3a.[50,52] In addition, jointly interpreting the nitrile's TDM and frequency using eq. 3a and eq. 2, respectively, enables quantification of the anomalous H-bonding blueshift $\Delta\bar{\nu}_{HB}$.[50]

In our recent study, we measured nitrile frequencies and TDMs to *directly* assess nitrile H-bonding blueshifts for the first time.[50] The new TDM-based method showed that $\Delta\bar{\nu}_{HB}$ can adopt values in a large range from 2 cm^{-1} to 22 cm^{-1} in distinct solvent or protein environments.[48,50,53] Consequently, we wondered whether the blueshift's magnitude could be a useful metric to describe H-bonding, that is, if $\Delta\bar{\nu}_{HB}$ in eq. 2 could be mathematically modelled. Previous theoretical work explored the complicated vibrational behavior of the C≡N group and suggested that the anomalous $\bar{\nu}/\vec{F}$-trend stems from nonnegligible higher order multipole effects[34] or from contributions due to Pauli repulsion.[38] Further, previous work[34,50] implied that $\Delta\bar{\nu}_{HB}$ may be a HB angle-dependent term (Fig. 1C), which would be consistent with both proposed physical origins. The lack of intuition for the blueshift's magnitude motivates the need to model $\Delta\bar{\nu}_{HB}$ in a physically interpretable form.

As such, we systematically explore HB blueshifts of the C≡N probe herein with the aim to find a simple, analytical expression for this observable. Towards this goal, we combined results from density functional theory (DFT)[55] and the AMOEBA polarizable force field[56] to generate a calibration for the vibrational response of the nitrile-containing molecule *o*-tolunitrile (oTN; see Fig. 1C). In this approach, DFT was used to obtain C≡N vibrational frequencies and TDMs in a large set of purely electrostatic and H-bonding environments (~ 1000 conditions) including point charges (Fig. 1D) and water and methanol (MeOH) molecules (Fig. 1E), respectively. Then, the corresponding electric fields exerted on the C≡N were derived from the AMOEBA force field. We attempted to recapitulate the DFT-based frequencies using the VSE (eq. 1a), which was (expectedly) unsuccessful due to the HB blueshift; in contrast, DFT TDMs are well-described by their corresponding VSE equation (eq. 3a), highlighting the different frequency/TDM behaviors that were experimentally observed (Fig. 1A, B).[50] We modelled the DFT-derived HB blueshift as a function of HB distance and angle and successfully formulated a quantitative "HB blueshift-vs-HB geometry" relationship. We demonstrate the applicability of

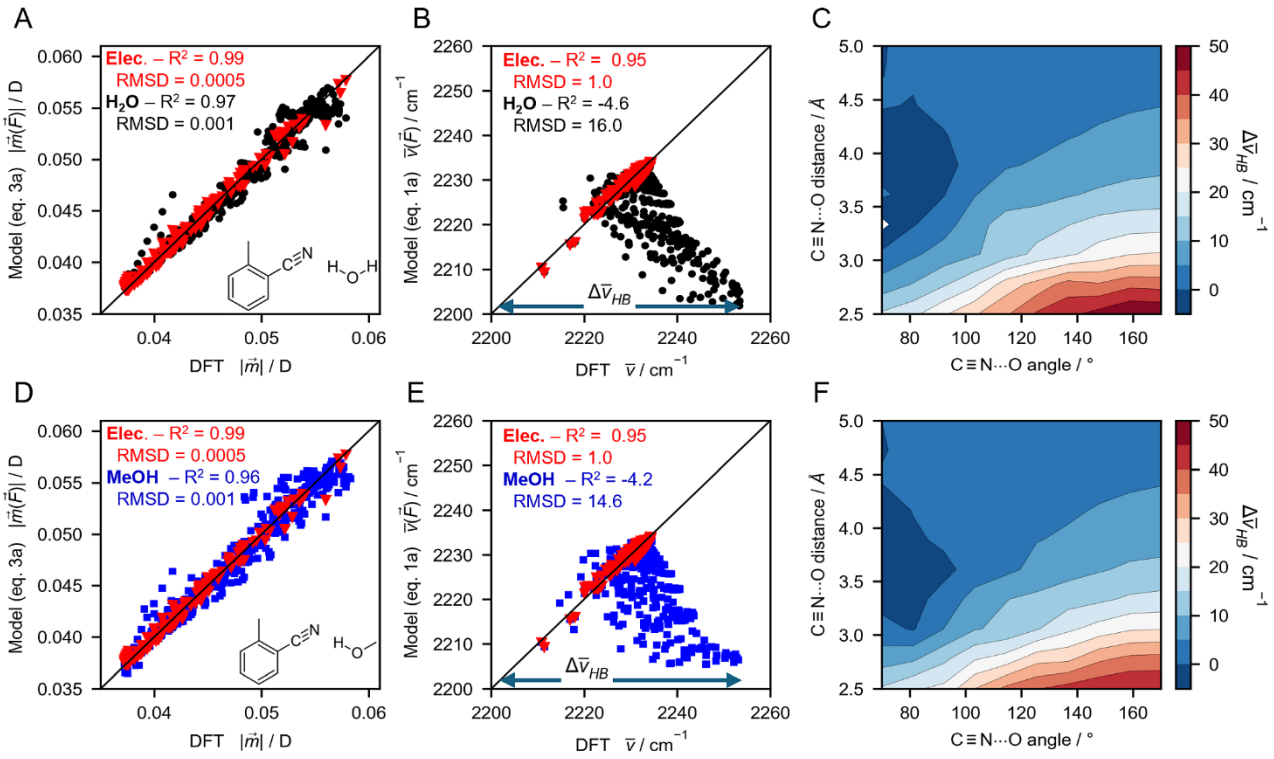

Figure 2. VSE modelling of DFT-based transition dipoles and vibrational frequencies (eq. 3a and eq. 1a, respectively; exact analytical forms are shown in eq. S1 and S2) for oTN's C≡N stretching mode in purely electrostatic environments with point charges and in H-bonding environments with water (A, B, C) and methanol (D, E, F). A, D: Correlation plots between modelled and DFT-based transition dipoles demonstrate eq. 3a accurately describes nitrile environments with purely electrostatic perturbations (red triangles in A and D), water as a HB donor (black circles in A), and methanol as a HB donor (blue squares in D). Fitting parameters for all three environments are reported in Table S1. B, E: Correlation plots between modelled and DFT-based vibrational frequencies indicate that eq. 1a only applies to nitriles under purely electrostatic perturbations (red triangles in B and E; fitting parameters reported in Table S2); when water or methanol are HB donors (black circles in B and blue squares in E, respectively), no correlation ($R^2 < 0$) is found. The HB blueshift, $\Delta\bar{\nu}_{HB}$, is determined as the difference between the DFT-predicted frequency and the black line representing ideal correlation, as indicated by the double headed horizontal arrows. C, F: 2D heat plots of $\Delta\bar{\nu}_{HB}$ dependence on heavy atom HB distance and angle [d(C≡N---$O_{water/MeOH}$) and θ(C≡N---$O_{water/MeOH}$)].

this relationship by comparison with experimentally derived blueshifts: we find that $\Delta\bar{\nu}_{HB}$ for nitriles with rigid HBs can directly report on HB geometries, while $\Delta\bar{\nu}_{HB}$ for nitriles with fluctuating HBs are approximately halved from values predicted using geometry due to motional narrowing.

RESULTS AND DISCUSSION

Modelling DFT-based frequencies and transition dipoles using the vibrational Stark effect

In order to find an empirical relation for the HB shift, we chose a DFT-based strategy in which individual positive point charges (125 cases; Fig. 1D) or individual water or methanol molecules (420 cases each; Fig. 1E) were placed around oTN's C≡N to model attractive purely electrostatic interactions or H-bonding interactions, respectively. These poses were optimized and normal mode analysis was performed to extract nitrile frequencies and TDMs (b3lyp/6-311++g** level of theory with GD3 dispersion correction). oTN was chosen as our model molecule because it is the sidechain fragment of the nonnatural amino acid *o*-cyanophenylalanine (oCNF), with which we previously developed and applied the new TDM-based analysis in solvent and protein environments.[50,52] The charges and molecules were positioned at $N_{C\equiv N}$-charge or $N_{C\equiv N}$-$O_{HB\ donor}$ distances (d), respectively, ranging from 5.0 – 8.0 Å for point charges and 2.5 – 5.0 Å for HB donors, and C≡N-charge and C≡N-$O_{HB\ donor}$ angles (θ) of 70 – 175° were used (Fig. 1C). The HB distance range was motivated by typical radial distribution functions of HBs, which have a first solvation sphere centered around 2.5 – 3.5 Å.[55] The angle range encapsulates HBs which vary from head-on (~ 180°) to side-on (~ 90°). Note that the ideal head-on angle of 180° was not used due to convergence issues in the DFT calculations. The DFT-derived vibrational frequencies ($\bar{\nu}$) and TDM magnitudes ($|\vec{m}|$) were scaled by 0.9598[56] or 0.4464, respectively, to match the experimental zero-field observables (see Methods Section).[50]

Using DFT, we obtained $|\vec{m}|$ and $\bar{\nu}$ values for oTN of 0.037 – 0.060 D and 2210 – 2255 cm^{-1}, respectively (see *x*-axes in Fig. 2A, B), which are consistent with prior experimental observations for aromatic nitriles (see Fig. 1A, B).[18,25,40,50,52,53] From the observed ranges it can be seen that

purely electrostatic and H-bonding environments give rise to similar values for $|\vec{m}|$ (Fig. 2A), consistent with eq. 3a's indication that $|\vec{m}|$ is only a function of $\vec{F}$. For the frequencies (Fig. 2B), purely electrostatic perturbations produce $\bar{\nu}$ values below the gas phase frequency of 2232 cm^{-1}, consistent with attractive electrostatic C≡N-charge interactions. In contrast, most H-bonding environments with water give rise to frequencies > 2232 cm^{-1}, indicative of the H-bonding blueshift.

To further underscore the difference in behavior exhibited by the frequencies vs the TDMs, we used the corresponding VSE equations including quadratic electric field contributions (eq. 1a and extension of eq. 3a; see eq. S2 and eq. S1, respectively) to model the DFT-based vibrational observables solely as functions of $\vec{F}$. Towards this goal, we used the polarizable AMOEBA force field[57] to extract the electric field vectors ($\vec{F}$) along the C≡N group for the DFT-optimized structures (see Experimental Section for further details). All VSE parameters were allowed to freely vary when fitting the VSE equations against the DFT results (see Tables S1 and S2). For the TDMs, we found that the VSE modelled the DFT results for purely electrostatic and H-bonding perturbations very well with R^2 > 0.97 (Fig. 2A). This is consistent with our previous experimental results that TDMs give direct access to the local nitrile electric field in both non-H-bonding and H-bonding environments (Fig. 1A).[50,52] Further, this modelling provides a good estimate of the experimental linear field sensitivity of $-1.0\frac{mD}{MV/cm}$ (as discussed in SI Section 2).[50]

In contrast to the TDMs, the C≡N vibrational frequency shifts are modelled well with eq. 1a for purely electrostatic perturbations but extremely poorly for nitriles with HBs to water molecules (Fig. 2B). For purely electrostatic perturbations, the correlation between the modelled and DFT frequencies is very good with R^2 of 0.95. This modelling resulted in a Stark tuning rate of $|\Delta\vec{\mu}| = 0.22\frac{cm^{-1}}{MV/cm}$ (Table S2), which is impressively close to the experimental value of $0.19\frac{cm^{-1}}{MV/cm}$.[50] However, when H-bonded data points are modelled with eq. 1a using the same parameters, an extremely poor correlation of R^2 = -4.6 is obtained, implying that eq. 1a provides a worse description than just modeling the data with its mean value. The bulk of the deviating data points are located below the line of perfect correlation, i.e. the DFT frequencies are larger than those predicted using eq. 1a. We interpret this deviation (along the x-axis in Fig. 2B) as the H-bonding blueshift $\Delta\bar{\nu}_{HB}$ (eq. 2; see Fig. 1A).

To verify that this behavior is not specific to water, we used methanol as an alternative HB donor; this is an important test, as methanol is a model for the amino acid sidechains of serine or threonine, and the largest experimentally observed $\Delta\bar{\nu}_{HB}$ occurred for a threonine–nitrile interaction.[50] We found that the VSE model's ability to recapitulate the DFT results for TDMs is just as robust as in the case where water is the HB donor (R^2 = 0.96, Fig. 2D), and highly similar VSE parameters were obtained to those derived for water H-bonding scenarios (Table S1). Yet, the correlation of VSE (eq. 1a) and DFT $\bar{\nu}$ values for nitriles with methanol HBs is just as poor as the case for water HBs (R^2 = -4.2, Fig. 2E).

Modelling the HB shift $\Delta\bar{\nu}_{HB}$ as a HB-geometry-dependent observable

In order to understand the unilateral deviation of the $\bar{\nu}$ values modelled with eq. 1a compared to the DFT frequencies in H-bonding conditions, we hypothesized that $\Delta\bar{\nu}_{HB}$ is a HB-geometry-dependent value, i.e. it depends on the HB-heavy atom distance d(C≡N---$O_{water/MeOH}$) and the HB-heavy atom angle θ(C≡N---$O_{water/MeOH}$) (d and θ in Fig. 1C). Note that we chose heavy atom-based distances and angles instead of the C≡N---$H_{water/MeOH}$ geometry used in other work[54,58] due to inaccuracies in hydrogen atom positions in MD simulations introduced by frequently used constraint algorithms;[59] furthermore, a calibration with heavy-atoms enables comparisons with protein crystal structures, where protons are very rarely resolved. Extracting the $\Delta\bar{\nu}_{HB}$ values from Fig. 2B and Fig. 2E and the corresponding d(C≡N---$O_{water/MeOH}$) and θ(C≡N---$O_{water/MeOH}$) from the DFT-optimized geometries, we can visualize the $\Delta\bar{\nu}_{HB}$ geometry dependences for water and methanol HBs as 2D heat plots in Fig. 2C and Fig. 2F, respectively. In both cases, we observe two trends: in going from short (2.5 Å) to long (5.0 Å) distances, $\Delta\bar{\nu}_{HB}$ decreases steadily towards zero, with slightly negative values at intermediate distances (3.5 – 4.0 Å) for side-on HBs (see transition from blue to dark blue to blue at angles of 70° – 90° and distances of 3.0 – 4.5 Å; Fig. 2C, F); at the same time, $\Delta\bar{\nu}_{HB}$ decreases while going from head-on (175°) to side-on HBs (70°).

Extracting the $\Delta\bar{\nu}_{HB}$ values for head-on or side-on HBs, we can quantify the distance-dependence of $\Delta\bar{\nu}_{HB}$. We combined the data sets for water and methanol HBs, and we found that head-on HBs (θ = 175°) demonstrate an asymptotic trend (Fig. 3A) which decays from ~ 50 cm^{-1} at 2.5 Å to ~ 5 cm^{-1} at 5.0 Å according to a power law

$$\Delta\bar{\nu}_{HB,head-on}(d) \propto \left(\frac{d}{d_0}\right)^{n_1} = f_{head-on}(d) \qquad (4)$$

with n_1 ≈ -4.0 (R^2 = 0.99). This distance dependence is reminiscent of the energetic contribution from dipole-quadrupole interactions, which have a d^{-4} distance dependence.[60] The result is therefore in line with previous interpretations of the $\Delta\bar{\nu}_{HB}$ describing higher (difference) multipole terms not included in the dipolar VSE equations (eqs. 1a/b).[34]

When evaluating side-on HBs (θ = 70°), we note a more complicated asymptotic distance dependence with a minimum at roughly 3.5 Å (as noted above), at which point $\Delta\bar{\nu}_{HB}$ is about -5 cm^{-1}; this is followed by a gradual increase of $\Delta\bar{\nu}_{HB}$ at larger d, becoming nearly negligible around 5.0 Å. We modelled this distance dependence with a Buckingham-like function (R^2 = 0.89),[61,62]

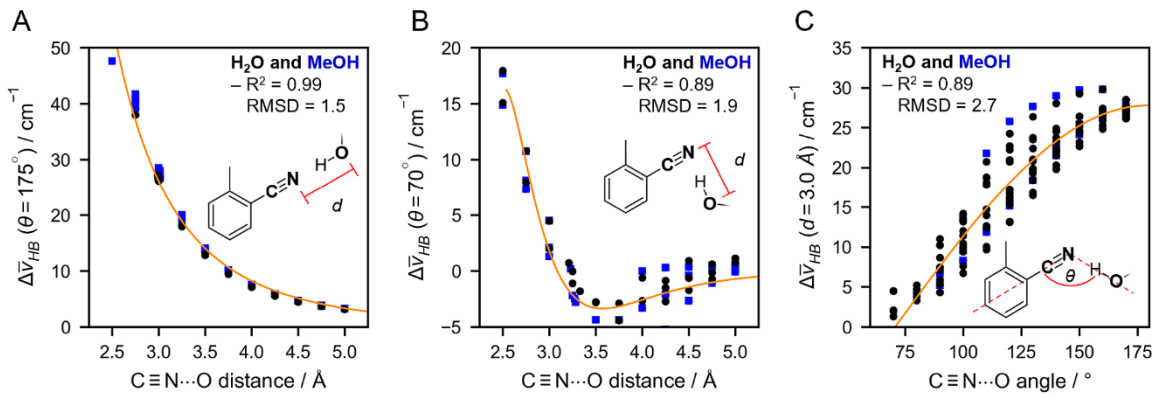

Figure 3. Models for $\Delta\bar{\nu}_{HB}$ dependence on HB distance and angle based on data from Fig. 2 C and F (black and blue data points for water and methanol as the HB donor to the nitrile, respectively). A: HB distance dependence of $\Delta\bar{\nu}_{HB}$ for head-on HBs (θ(C≡N---O$_{water/MeOH}$) = 175°) can be modelled with an asymptotic form $\Delta\bar{\nu}_{HB}(d) \propto d^{n_1}$, with $n_1 = -4.03$ (R^2 = 0.99 and RMSD = 1.5 cm^{-1}). B: HB distance dependence of $\Delta\bar{\nu}_{HB}$ for side-on HBs (θ(C≡N---O$_{water/MeOH}$) = 70°) is modelled with a Buckingham-like function $\Delta\bar{\nu}_{HB}(d) \propto \exp\left(-b(d-d_0)\right) - (d/d_0)^{n_2}$, with $b = -3.1$ Å^{-1}, $n_2 = -8.2$, and $d_0 = 3.09$ (R^2 = 0.89 and RMSD = 1.9 cm^{-1}). Note that the Buckingham potential becomes unphysical at distances < 2.5 Å and therefore is not shown. C: HB angle dependence of $\Delta\bar{\nu}_{HB}$ at a constant HB distance d(C≡N---O$_{water/MeOH}$) = 3.0 Å can be modelled using $\Delta\bar{\nu}_{HB}(\theta) \propto \cos[m \cdot (\theta - 180°)]$ with $m = 0.82$ (R^2 = 0.89 and RMSD = 2.7 cm^{-1}). See Table S3 for the complete list of optimized parameters.

$$\Delta\bar{\nu}_{HB,side-on}(d) \propto e^{-b(d-d_0)} - \left(\frac{d}{d_0}\right)^{n_2} = f_{side-on}(d) \qquad (5)$$

which described the well at ~ 3.5 Å more accurately than Lennard-Jones, Morse, or buffered 7-14 shapes (see Fig. S1). We extracted values for the exponential decay constant (b) and the exponent of the power-term (n_2) of $b \approx 3.1$ Å^{-1} and $n_2 \approx -8.2$. The decay constant is in a similar range as values used for intermolecular O---C, C---H, and O---H interactions in force fields (a range of 2.7 – 4.6 Å^{-1}),[63] suggesting that HB blueshifts in side-on HBs originate from Pauli repulsion; this finding is consistent with previous studies.[38] The power law in the Buckingham potential is typically used with an exponent of -6 to account for attractive dipole – induced dipole interactions. However, the original form of the Buckingham potential also included a d^{-8}-term accounting for attractive quadrupole – induced quadrupole interactions.[61,62] When fitting the data in Fig. 3B using two power-terms, both exponents converged to the same value of ~ -8.2, indicating this value is fairly robust; as such, we tentatively assign negative contributions to $\Delta\bar{\nu}_{HB}$ (i.e., redshifts) to induced higher-order multipole interactions.

In a similar fashion, we extracted the angular dependence of $\Delta\bar{\nu}_{HB}$ at a HB distance of 3.0 Å, the average HB distance found in solvents and proteins (Fig. S5-S6; Table S6) and the distance where the side-on HB effect should be close to negligible (see Fig. 3B). We used the relation

$$\Delta\bar{\nu}_{HB,head-on}(\theta) \propto \cos[m \cdot (\theta - 180°)] = f(\theta) \qquad (6)$$

to model the data points, and the best fit yielded m = 0.82 (R^2 = 0.89), which accounts for the zero crossing at ~ 70° (Fig. 3B) by altering the cosine period. This deviation from m = 1 can be understood when taking into account that a side-on HB interacting with the π-orbitals of the C≡N would occur at θ(C≡N---O$_{water/MeOH}$) ≈ 70° - 80° (Fig. S2), and this is the point at which the cosine function should be 0.

Combining these dependencies, we now propose a HB-geometry-dependent relationship for $\Delta\bar{\nu}_{HB}$ composed of eqs. 4, 5, and 6 with the exponents set to integer values n_1 = -4 and n_2 = -8:

$$\Delta\bar{\nu}_{HB}(d,\theta) =$$

$$\Delta\bar{\nu}_{HB,0} \cdot \{f_{head-on}(d) \cdot f(\theta) + f_{side-on}(d) \cdot [1 - f(\theta)]\} \qquad (7)$$

$$= \Delta\bar{\nu}_{HB,0} \cdot \left\{\left(\frac{d}{d_0}\right)^{-4} \cdot \cos[m \cdot (\theta - 180°)] + \left[e^{-b(d-d_0)} - \left(\frac{d}{d_0}\right)^{-8}\right] \cdot [1 - \cos[m \cdot (\theta - 180°)]]\right\}$$

Here, $\Delta\bar{\nu}_{HB,0}$ is the HB blueshift at a reference distance d_0, chosen as the point at which the Buckingham shape crosses zero. Further, $f(\theta)$ is the angular term in eq. 6 which modulates the contributions of the head-on and side-on distance dependences of eq. 4 and 5, respectively. We modelled the C≡N frequency for nitriles experiencing purely electrostatic perturbations, HBs with water, and HBs with methanol simultaneously as a function of electric field, HB distance, and HB angle, i.e., using eq. 2 with eq. 7 for the $\Delta\bar{\nu}_{HB}$ term. The resulting "$\bar{\nu}(\vec{F}, d, \theta)$ model vs DFT" plot (Fig. 4A) shows that the VSE (eq. 1a) with the addition of eq. 7 recapitulates the DFT frequencies for purely electrostatic environments just as well as the VSE model alone (Fig. 2B, E) but significantly improves the recapitulatability in H-bonding environments.

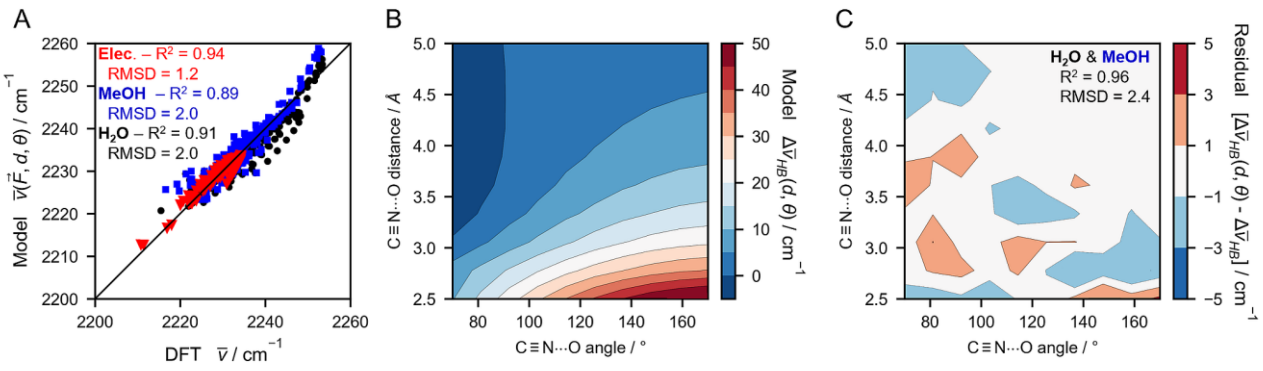

Figure 4. DFT-based vibrational frequencies for oTN's C≡N stretching mode are recapitulated well when modelled as a function of electric field, HB distance, and HB angle. A: Correlation plot of $\bar{\nu}(\vec{F}, d, \theta)$ modelled (eq. 2 utilizing eq. 1a and eq. 7) and DFT-based vibrational frequencies shows that the model applies equally well for purely electrostatic perturbations (red triangles) and in the presence of water and methanol HBs (black circles and blue squares, respectively) with an overall R^2 = 0.92 and RMSD = 1.8 cm^{-1} (R^2 and RMSD values for each distinct environment are shown in the graph). Fitting parameters for the model are reported in Table 1 and Table S4. B: 2D heat plot of $\Delta\bar{\nu}_{HB}(d,\theta)$ with water and methanol as HB donors according to the model in eq. 7. C: 2D heat plot of the residuals between modelled $\Delta\bar{\nu}_{HB}(d,\theta)$ (see B) and $\Delta\bar{\nu}_{HB}$ from Fig. 2 C and F (R^2 = 0.96 and RMSD = 2.4 cm^{-1}).

Specifically, the fitting quality was effectively unaltered for purely electrostatic perturbations (from R^2 = 0.95 to 0.94) but drastically improved in H-bonding environments (from R^2 < 0 to ~0.9). In this fit, the previously optimized VSE and empirical H-bonding parameters remain similar to those obtained in Fig. 2 and Fig. 3 with $|\Delta\vec{\mu}| = 0.22\frac{cm^{-1}}{MV/cm}$, a side-on exponential decay constant of b = 2.85 $Å^{-1}$, and a cosine period modulation of m = 0.91. When we visualized the dependence of $\Delta\bar{\nu}_{HB}(d, \theta)$ in eq. 7 on d(C≡N---$O_{water/MeOH}$) and θ(C≡N---$O_{water/MeOH}$) as a 2D heat plot (Fig. 4B), we found a highly analogous profile to those in Fig. 2C and Fig. 2F with a similarly broad range of values adopted (-5 – 50 cm^{-1}), showing that eq. 7 can recapitulate the DFT HB blueshifts with high accuracy. A 2D heat plot of the residuals between $\Delta\bar{\nu}_{HB}(d, \theta)$ (eq. 7) and $\Delta\bar{\nu}_{HB}$ obtained from DFT (Fig. 2 C, F) has residual values ranging from just -3 to +3 (Fig. 4C; R^2 = 0.96), further indicating eq. 7 accurately describes the blueshift for many HB distance and angle combinations. Some of the largest residuals are found for angles corresponding with side-on HBs, where the Buckingham potential slightly underestimates $\Delta\bar{\nu}_{HB}$ (Fig. 3B). Even though eq. 7 takes the form of a lengthy expression, only four parameters are needed to sufficiently tune the distance and angle dependence (Table 1), and all of them carry physical meaning in terms of describing specific underlying intermolecular interactions.

As shown in SI Section 6, we narrowed down Fig. 4B to a relevant regime of commonly adopted HB geometries in solvents for heavy atom distances of < 3.5 – 4.0 Å. Based on AMOEBA MD simulations of oTN in water and methanol (see details in SI Section 1), the average HB distance decreases monotonically from 3.35 Å for side-on HBs (70°) towards 2.93 Å when head-on HBs are adopted. Our model (eq. 7) predicts $\Delta\bar{\nu}_{HB}$ ≈ -5 cm^{-1} for side-on HBs interacting with the C≡N's π-orbitals [~ 70° for θ(C≡N---O)]. As the angle and distance concomitantly increase and decrease, respectively, the blueshift increases steadily, plateauing around 26 cm^{-1} for head-on HBs with θ(C≡N---O) > 170°. Furthermore, we also investigated the HB blueshift in the (rare) case of two simultaneous HBs with a nitrile by comparing DFT blueshifts with values derived using eq. 7 (SI Section 5): we found that summing $\Delta\bar{\nu}_{HB}$ for each HB was an accurate model, implying each H-bonding interaction can be treated independently.

Table 1. Optimized parameters for the HB geometry-dependent model in eq. 7 describing the HB blueshift in Fig. 4B. The corresponding VSE parameters are shown in Table S4.

Parameters	Optimized values
$\Delta\bar{\nu}_{HB}$ parameters:	
d_0 / Å	3.36 ± 0.03
$\Delta\bar{\nu}_{HB}$ / cm^{-1}	16.6 ± 0.6
b / $Å^{-1}$	2.85 ± 0.14
m	0.91 ± 0.01

Testing the HB-geometry-dependent model for $\Delta\bar{\nu}_{HB}$ against experimental data

Based on the HB geometry-dependent model's ability to recapitulate the nitrile DFT frequencies, we sought to test the model by comparing predicted blueshifts against experimental data for cases with nitriles in H-bonded environments. Towards this goal, we revisited our recent work, in which we introduced the noncanonical amino acid oCNF into photoactive yellow protein (PYP).[50,52] In this previous work, oCNF was incorporated into PYP in place of endogenous phenylalanines (F), resulting in two PYP variants, F92oCNF and F28oCNF, which were H-bonded and showed distinct $\Delta\bar{\nu}_{HB}$ values with moderate to large magnitudes.

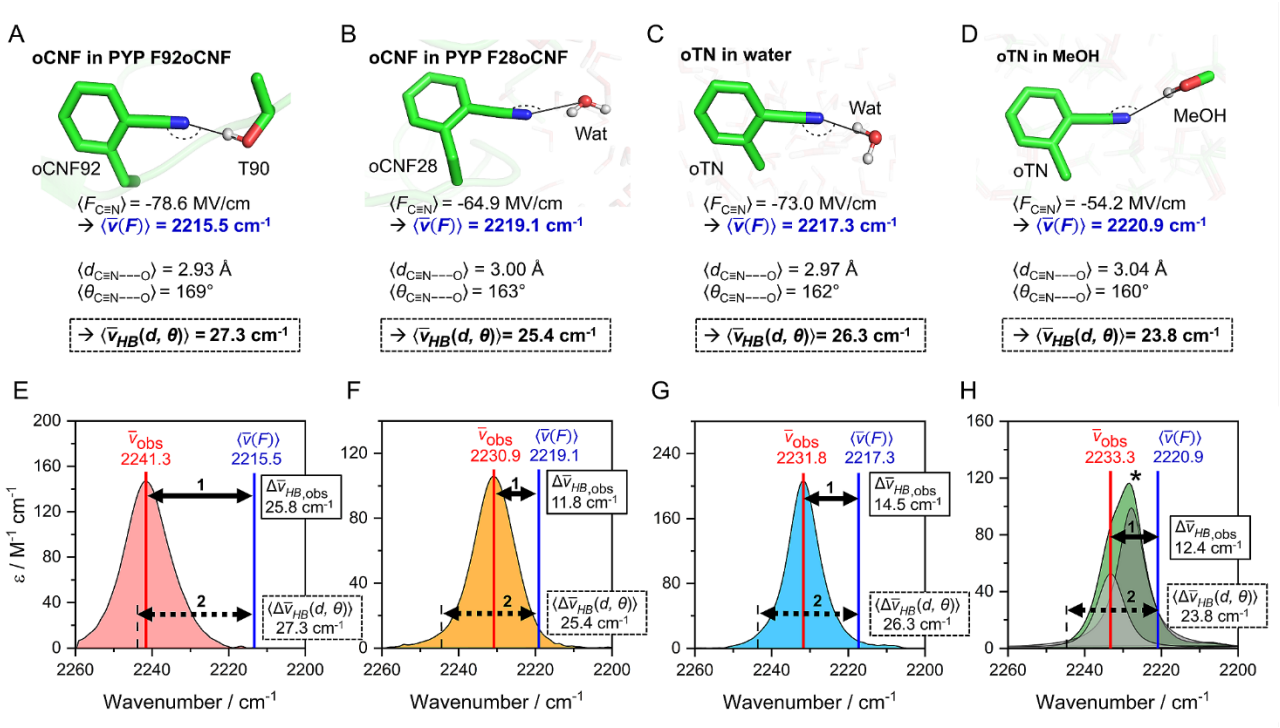

Figure 5. Testing the HB geometry-dependent model $\Delta\bar{\nu}_{HB}(d,\theta)$ against experimentally observed blueshifts for nitriles in proteins and solvents. A, B, C, D: Representative C≡N H-bonding AMOEBA MD structures of noncanonical amino acid oCNF in PYP variants F92oCNF (A) and F28oCNF (B) and of oTN in water (C) and methanol (D). Average electric fields on the C≡N in H-bonding fractions from MD simulations are shown below the structures,[52] and the resulting VSE-based frequencies $\langle\bar{\nu}(F)\rangle$ (eq. 1b) are shown highlighted in blue. Further below, average HB donor distances and angles from the simulations[52] are shown together with the resulting average HB blueshift $\langle\Delta\bar{\nu}_{HB}(d,\theta)\rangle$ (eq. 7) in a dashed-line box. E, F, G, H: Experimental determination of $\Delta\bar{\nu}_{HB,obs}$ using IR spectra of F92oCNF (E), F28oCNF (F), oTN in water (G) and oTN in methanol (H). The peak position is specified by a solid red line labelled with $\bar{\nu}_{obs}$. C≡N frequencies due to the VSE alone are indicated by a blue vertical line labelled with $\langle\bar{\nu}(F)\rangle$ (see also A – D). The difference between $\bar{\nu}_{obs}$ and $\langle\bar{\nu}(F)\rangle$, i.e. between the red and blue lines, is indicated by a solid double headed arrow (1) representing the experimentally observed HB blueshift $\Delta\bar{\nu}_{HB,obs}$. The dashed double headed arrow (2) represents the predicted HB blueshift $\langle\Delta\bar{\nu}_{HB}(d,\theta)\rangle$ in A – D. For oTN in methanol (H), only the H-bonding fraction is evaluated (the non-H-bonding band is indicated by an asterisk; see SI Section 9 for more details). Data in E – G are reproduced from ref. [50]. Copyright 2022 American Chemical Society.

In the following, we reanalyze our previously obtained data (namely, IR spectra, crystal structures, and MD simulations) to enable comparisons between experimentally derived HB blueshifts ($\Delta\bar{\nu}_{HB,obs}$) and HB blueshifts predicted from MD simulations using eq. 7 (i.e., $\Delta\bar{\nu}_{HB,}(d,\theta)$).[50]

Starting with F92oCNF (Fig. 5A), x-ray crystallography showed that the C≡N group is engaged in a head-on HB with the hydroxyl group of threonine 90 (T90), and 100 ns long AMOEBA MD simulations indicated an average C≡N---HO-T90 HB distance and angle of 2.93 Å and 169°, respectively (see Fig. 5A, a representative MD snapshot).[50,52] Using the HB geometry-dependent model in eq. 7, we derive an average predicted value of $\langle\Delta\bar{\nu}_{HB,}(d,\theta)\rangle$ = 27.3 cm^{-1}, a large value as expected for a head-on HB (Fig. 4B). To compare this value to experimental results (Fig. 5E), we also determined the C≡N's peak position due to the VSE alone (eq. 1b); this was done by using the experimentally-determined zero-field frequency and Stark tuning rate[50] and the average electric field for the H-bonding fraction from MD (-78 MV/cm, ref. [52]; see SI Section 9 for further details). We obtain a VSE-based vibrational frequency of 2215.5 cm^{-1} (blue values in Fig. 5A/Fig. 5E and vertical blue line in Fig. 5E). The experimental IR spectrum of F92oCNF has a peak position of 2241.3 cm^{-1},[50] and subtracting the frequency for the VSE alone from the experimental frequency results in a HB blueshift of $\Delta\bar{\nu}_{HB,obs}$ = 25.8 cm^{-1} (eq. 2). This experimentally derived blueshift matches very well with the HB geometry-based value of 27.2 cm^{-1}, as indicated by the similar length of the solid and dashed double headed arrows in Fig. 5E. We note that similar results are obtained when $\langle\Delta\bar{\nu}_{HB,}(d,\theta)\rangle$ is calculated from the distribution of $\Delta\bar{\nu}_{HB,}(d,\theta)$ values obtained by applying eq. 7 to each H-bonding frame of the MD simulation (see distributions for this and the following cases in Fig. S12).

Further support for our HB geometry-based $\Delta\bar{\nu}_{HB,}(d,\theta)$ model and the observation of large values for head-on and/or short HBs is provided by a new publication where a nitrile probe was incorporated into different metal organic frameworks (MOFs).[64] The rigid MOF structure enabled the introduction of H-bonding moieties (allylic and aromatic carboxylic acids) near the nitrile. According to DFT, these C≡N---HO interactions occur at average HB

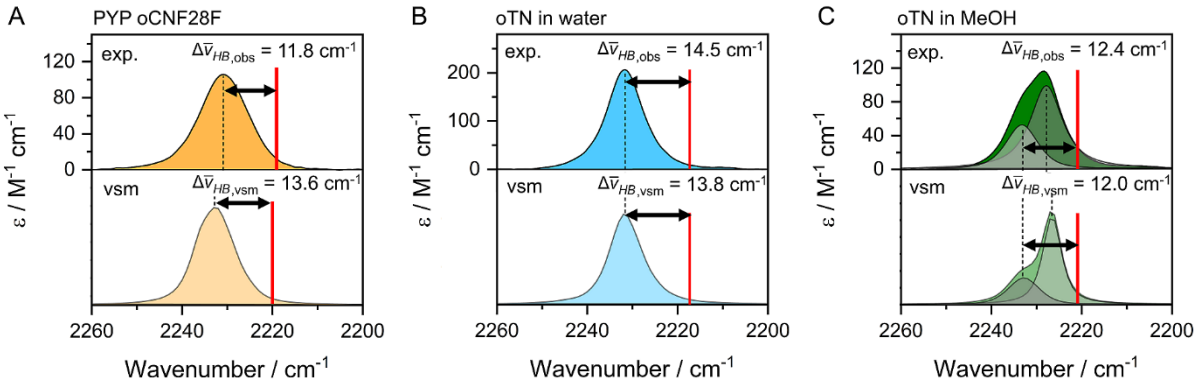

Figure. 6: HB blueshifts for nitriles exposed to solvent environments are modulated by dynamics, i.e. HB fluctuations. A, B, C: Top row shows experimental IR spectra for the C≡N stretch in PYP F28oCNF (A), oTN in water (B) and oTN in methanol (C) as shown in Fig. 5 F, G, and H, respectively. The bottom row shows corresponding MD-based simulated IR spectra using eq. 2 (with eqs. 1a and 7) and parameters in Table 1 (and Table S4) as a vibrational spectroscopic map (vsm) obtained using the fluctuating frequency approximation (see Methods Section). The solid red vertical lines are predicted peak positions due to the VSE only (using eq. 1b and parameters from ref. [50]) in Fig. 5 F, G, and H, and the blueshifts derived from the vsm ($\Delta\bar{\nu}_{HB,vsm}$) are the difference between the simulated peak position and the frequency of the red line. Data in A is reproduced from ref. [50]. Copyright 2022 American Chemical Society.

distances/angles of 2.85 Å/168° (allylic acid; "AA"), 2.80 Å/148° (benzoic acid; "CPh"), and 2.79 Å/150° (isophthalic acid; "DCPh"). As in the case of F92oCNF, $\Delta\bar{\nu}_{HB,obs}$ and $\langle\Delta\bar{\nu}_{HB,}(d,\theta)\rangle$ are in excellent agreement: the experimental/predicted values (in cm^{-1}) for AA are 36/31.8, for CPh are 29/28.2, and for DCPh are 33/32.2. It is interesting to note that the nitrile in the MOFs is an aliphatic C≡N, not an oTN derivative, and that the nitrile HB partners are carboxylic acids, not water or alcohols. These differences make the similarity between the experimental and our predicted HB shifts all the more impressive; this comparison suggests that our model can work generally for H-bonded nitriles with different types of HB donors.

We next analyzed F28oCNF, where crystallography showed that the C≡N group is solvent exposed and H-bonded to bulk water;[50] MD indicated this interaction has an average HB distance and angle of 3.00 Å and 163° (Fig. 5B).[52] Using eq. 7, we obtained $\langle\Delta\bar{\nu}_{HB,}(d,\theta)\rangle$ = 25.4 cm^{-1} (Fig. 5B). However, unlike F92oCNF, we noted a considerable discrepancy between this value and $\Delta\bar{\nu}_{HB,obs}$ when we analyzed F28oCNF's IR spectra (Fig. 5F). F28oCNF has an average electric field of -64.9 MV/cm in the MD H-bonding fraction (see ref. [52]), and the pure VSE effect predicts the C≡N's peak position to be at 2219.1 cm^{-1} (see values in Fig. 5B and red line in Fig. 5F). However, in the experimental IR spectrum, we observe a peak position at 2230.9 cm^{-1}, which leads to $\Delta\bar{\nu}_{HB,obs}$ = 11.8 cm^{-1}, only half as large as $\langle\Delta\bar{\nu}_{HB,}(d,\theta)\rangle$ (this is visually demonstrated in Fig. 5F by the red line appearing halfway along the dashed double headed arrow). We hypothesized that this discrepancy may be related to F28oCNF's H-bonding with the highly fluctuating solvent environment, in which the C≡N rapidly alternates between H-bonding and non-H-bonding states (SI Section 8).

To test this idea, we analyzed the HB shifts for our model molecule oTN in water and methanol. From AMOEBA MD simulations, we find that oTN adopts similar HB geometries as F28oCNF, i.e. an average HB distance and angle of ~ 3.0 Å and ~ 160° with the nitrile (Fig. 5C and D for water and methanol, respectively). Using eq. 7, we obtain relatively large $\langle\Delta\bar{\nu}_{HB,}(d,\theta)\rangle$ values, with 26.3 cm^{-1} in water and 23.8 cm^{-1} in methanol (Fig. 5C, D). Extracting $\Delta\bar{\nu}_{HB}$ experimentally, we obtain $\Delta\bar{\nu}_{HB,obs}$ values of 15.2 and 13.1 cm^{-1}(Fig. 5G and H, respectively), indicating $\Delta\bar{\nu}_{HB,obs}$ is again much smaller than $\langle\Delta\bar{\nu}_{HB,}(d,\theta)\rangle$ like for F28oCNF. Note that in methanol (Fig. 5H), H-bonded and non-H-bonded oTN populations are detected as two overlapping peaks (2233.3 and 2227.8 cm^{-1}); we herein discuss only the H-bonded fraction (see SI Section 9 and Fig. S10).

To reconcile the excellent match for F92oCNF and the MOFs but the disparity for F28oCNF and oTN in solvents, we must take into consideration the time scales under which HBs fluctuate for both groups. In F92oCNF (Fig. 5A), the C≡N is engaged in an intra-protein HB: we detect extended periods of uninterrupted H-bonding and narrow HB distance and angle distributions in AMOEBA MD simulations (see SI Sections 7 and 8), indicating this HB experiences long residence times and minimal geometrical fluctuations. Because of this weakly fluctuating (rigid) C≡N---HO-T90 interaction, the $\Delta\bar{\nu}_{HB}$ distribution (Fig. 5E) directly reflects on the HB geometry as derived by our model in eq. 7 and Fig. 4B. The same argument holds true for the MOFs, where the HB geometry is locked in place by the framework. These cases are classified as the *inhomogeneous limit* in IR spectroscopy,[65] i.e. where IR spectra directly reflect the distribution of instantaneous vibrational frequencies. Instead, for F28oCNF and oTN in solvents, the H-bonding with bulk solvent is highly fluctuating, characterized in MD by short H-bonding residence times and broad HB distance/angle distributions (SI Sections 7 and 8). If these fluctuations are faster than the difference in the vibrational frequencies between the fluctuating sub-states (a vibrational frequency difference of ~ 20 cm^{-1} corresponds to a time scale of ~ 2 ps), the sub-states are not resolved in the IR spectrum but instead motionally narrowed towards one IR

band with an averaged peak position[65] (as occurs in coalescence in nuclear magnetic resonance)[66]; lifetimes for H-bonding and non-H-bonding nitrile states were extracted from MD simulations and qualitatively support this possibility (Fig. S7 and Table S7).

One way to test the hypothesis of motional narrowing is by applying IR lineshape theory.[65,67] Accordingly, we used the parameters obtained from DFT to describe the C≡N transition dipole and frequency in terms of electrostatics and HB-geometry (Table 1 and Table S4; eqs. 1, 2, 3, and 7) as a model to compute theoretical IR spectra from AMOEBA MD trajectories (referred to as a vibrational spectroscopic map, or "vsm").[31] Towards this goal, we first calculated the instantaneous C≡N transition dipoles and frequencies from MD simulations (performed with 20 fs time steps over 2 ns in aggregate) for oTN in water and methanol and F28oCNF, and we utilized the well-documented fluctuating frequency approximation (FFA)[67,68] to calculate MD-based IR spectra. In FFA, a Fourier transformation of the auto-correlation of dipole and frequency fluctuations is used to calculate realistic lineshapes (eq. S3).[67,68] Comparing the resulting computed IR spectra of oTN in water and methanol (Fig. 6B and C, respectively) with those from experiment, we observe a very good recapitulation. In water, the simulated spectra yield one symmetric band for the C≡N stretch, with a peak position (2232 cm^{-1}) almost identical to the experimental value; in methanol, the FFA-based spectra show an asymmetric lineshape which occurs due to distinct H-bonded and non-H-bonded fractions absorbing at ~2233 and ~2228 cm^{-1}, respectively, which are again quite similar for experimental and computed spectra. Importantly, we can take the difference between the vsm frequencies and the previously determined frequencies due to the VSE alone (Fig. 5 G, H; red lines in Fig. 6B, C) to determine apparent $\Delta\bar{\nu}_{HB,vsm}$ values of 14.5 and 12.7 cm^{-1} for water and methanol, respectively, which deviate from the experimentally obtained values by < 0.7 cm^{-1}, an impressively close match. We used the same approach to calculate the IR spectrum and vsm blueshift for F28oCNF (Fig. 6A) and again obtain a good match for $\Delta\bar{\nu}_{HB}$: comparing $\Delta\bar{\nu}_{HB,obs}/\Delta\bar{\nu}_{HB,vsm}$, we observe values of 11.8/13.6 cm^{-1}, i.e. a deviation of only 1.8 cm^{-1}.

Overall, the vsm can recapitulate the experimental nitrile spectra with high accuracy. This demonstrates that our HB geometry-dependent model is not only robust in minimally fluctuating settings, but also in (quickly) fluctuating solvent or protein environments when dynamical effects are considered. More specifically, in the cases we tested with fluctuating HBs, the geometry dependent values of $\langle\Delta\bar{\nu}_{HB,}(d,\theta)\rangle$ = 23.8 – 26.3 cm^{-1} (Fig. 5 F – H) are reduced by a factor of roughly 2 to $\Delta\bar{\nu}_{HB,obs} \approx \Delta\bar{\nu}_{HB,vsm}$ = 11.8 – 15.2 cm^{-1} (Fig. 6 A - C). This reduction by a factor of 2 is what is expected for the simplest case when nitrile protic/aprotic sub-populations are interconverting with similarly fast exchange rates such that the geometry dependent value $\langle\Delta\bar{\nu}_{HB,}(d,\theta)\rangle$ will be averaged with 0 cm^{-1} (i.e., the blueshift for the non-H-bonded fraction). This exercise makes clear that knowledge of the dynamics experienced by a nitrile is key to prevent erroneous assessments of the HB geometry based on $\Delta\bar{\nu}_{HB,obs}$ alone: such dynamics can be evaluated using temperature dependent or two-dimensional IR experiments.[41,44,58,69]

To summarize the evaluation of our models for HB blueshifts, we correlated the experimental and predicted values for $\Delta\bar{\nu}_{HB}$ in Fig. 7. We find that calculating $\langle\Delta\bar{\nu}_{HB,}(d,\theta)\rangle$ from our HB geometry-dependent model in eq. 7 works very well for rigid HBs in F92oCNF and MOFs, implying it is possible to extract information on HB geometry directly from HB blueshifts. For fluctuating HBs like F28oCNF and oTN in solvents, HB dynamics have to be considered, as described above: when they are, an excellent agreement between observed and modelled HB blueshifts is obtained (R^2 = 0.95).

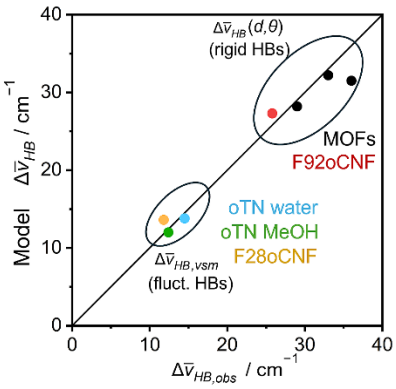

Figure. 7: Experimentally derived HB blueshifts of nitriles can be recapitulated by accounting for HB geometry and dynamics. The panel shows a correlation between experimentally observed ($\Delta\bar{\nu}_{HB,obs}$) and predicted ($\langle\Delta\bar{\nu}_{HB}(d,\theta)\rangle$) or simulated ($\Delta\bar{\nu}_{HB,vsm}$) blueshifts; when the appropriate model is used, the correlation is excellent (R^2 = 0.95). The black diagonal is the perfect correlation with a slope of 1. Black data points for MOFs are taken from ref. [64].

CONCLUSIONS

Aiming to provide a simple, empirical description for the anomalous HB blueshift of nitriles, we developed a model that describes HB effects on C≡N frequencies as the sum of the widely used VSE and an additional term, $\Delta\bar{\nu}_{HB}$. This model describes $\Delta\bar{\nu}_{HB}$ in terms of HB geometry, i.e. HB heavy atom distance *d*(C≡N---Donor) and angle *θ*(C≡N---Donor). The physical basis for the distance and angle dependence are a combination of repulsive quadrupolar electrostatic interactions for head-on HBs and an interplay between Pauli repulsion and attractive multipolar interactions for side-on HBs, supporting previous interpretations of the blueshift's origin(s).[34,70] These findings further expand on theoretical models that have aimed to understand H-bonding in terms of its quantum and/or classical mechanical nature, many of which have pointed towards a dominant (classical) electrostatic character;[71–73] our study is in line with this latter view. We found an important third contributor to $\Delta\bar{\nu}_{HB}$, the HB dynamics, also needs to be considered when using the model developed herein. $\Delta\bar{\nu}_{HB}$ values of rigid HBs with long

residence times and minimal fluctuations are directly dependent on HB geometry; in contrast, nitrile IR bands for quickly fluctuating HBs experience motional narrowing, altering their lineshapes. Consequently, HB residence/exchange times should be considered when estimating HB geometry via $\Delta\bar{\nu}_{HB}$. In closing, we emphasize that the nitrile model presented in eq. 7 works well for MOFs which have a different type of nitrile and different HB donors. This suggests that the model developed here is broadly applicable and can be used to characterize HBs for nitriles on diverse substrates, ranging from drugs to amino acids, and in diverse settings, ranging from electrodes to microdroplets to proteins.[19,20,37,42,44,50,52,58,74]

ACKNOWLEDGEMENTS

We would like to thank Srijit Mukherjee (Stanford University, USA) and Patrycja Kielb (Universität Bonn, Germany) for a close reading and helpful feedback on our manuscript. The authors thank the HPC Service of ZEDAT (Freie Universität Berlin) for computing time (10.17169/refubium-26754) and Steven G. Boxer (Stanford University, USA) for support and access to data from previous work.[50,52] J.M.K. was supported by a Burt and Deedee McMurtry Stanford Graduate Fellowship and a NIH grant (R35GM118044, to Steven G. Boxer). J.K. acknowledges the German Research Foundation (DFG) for financial support via the DFG Individual Research Grant KO 5464-4 (493270578) and the Sonderforschungsbereich SFB1078 project B9 (221545957).

SUPPORTING INFORMATION

The supporting information contains the Experimental Section as well as further sections detailing and summarizing the fitting results from Figure 2, alternative models for Figure 3, explanation on the parameter *m* in equation 7, modelling of two simultaneous HBs, HB radial distribution function from MD simulations of oTN, HB geometry and fluctuation analysis for oTN (in water and MeOH) and oCNF (F28oCNF and F92oCNF variants of PYP), further explanations for the determination of HB blueshifts and the calculation of IR spectra from MD simulations, and HB blueshifts determined by applying equation 7 to each MD frame. Additional references are cited in the supporting information.[14,16,29,32,50,52,56,57,75–88]

REFERENCES

(1) Perrin, C. L.; Nielson, J. B. "Strong" Hydrogen Bonds in Chemistry and Biology. *Annu. Rev. Phys. Chem.* **2003**, *48*, 511–544.
(2) Karas, L. J.; Wu, C. H.; Das, R.; Wu, J. I. C. Hydrogen Bond Design Principles. *Wiley Interdiscip. Rev. Comput. Mol. Sci.* **2020**, *10*, e1477.
(3) Sijbesma, R. P.; Meijer, E. Self-Assembly of Well-Defined Structures by Hydrogen Bonding. *Curr. Opin. Colloid Interface Sci.* **1999**, *4*, 24–32.
(4) Wasio, N. A.; Quardokus, R. C.; Forrest, R. P.; et al. Self-Assembly of Hydrogen-Bonded Two-Dimensional Quasicrystals. *Nature* **2014**, *507*, 86–89.
(5) Bolen, D. W.; Rose, G. D. Structure and Energetics of the Hydrogen-Bonded Backbone in Protein Folding. *Annu. Rev. Biochem.* **2008**, *77*, 339–362.
(6) Kool, E. T. Hydrogen Bonding, Base Stacking, and Steric Effects in DNA Replication. *Annu. Rev. Biophys.* **2003**, *30*, 1–22.
(7) Shan, S. O.; Herschlag, D. Hydrogen Bonding in Enzymatic Catalysis: Analysis of Energetic Contributions. *Methods Enzymol.* **1999**, *308*, 246–276.
(8) Schreiner, P. R. Metal-Free Organocatalysis through Explicit Hydrogen Bonding Interactions. *Chem. Soc. Rev.* **2003**, *32*, 289–296.
(9) Xiang, S. H.; Tan, B. Advances in Asymmetric Organocatalysis over the Last 10 Years. *Nat. Commun. 2020 111* **2020**, *11*, 1–5.
(10) Forbes, K. C.; Jacobsen, E. N. Enantioselective Hydrogen-Bond-Donor Catalysis to Access Diverse Stereogenic-at-P(V) Compounds. *Science* **2022**, *376*, 1230–1336.
(11) Cleland, W. W.; Kreevoy, M. M. Low-Barrier Hydrogen Bonds and Enzymic Catalysis. *Science* **1994**, *264*, 1887–1890.
(12) Dai, S.; Funk, L. M.; von Pappenheim, F. R.; et al. Low-Barrier Hydrogen Bonds in Enzyme Cooperativity. *Nature* **2019**, *573*, 609–613.
(13) Wang, L.; Fried, S. D.; Boxer, S. G.; et al. Quantum Delocalization of Protons in the Hydrogen Bond Network of an Enzyme Active Site. *Proc. Natl. Acad. Sci. USA* **2014**, *111*, 18454–18459.
(14) Fried, S. D.; Boxer, S. G. Measuring Electric Fields and Noncovalent Interactions Using the Vibrational Stark Effect. *Acc. Chem. Res.* **2015**, *48*, 998–1006.
(15) Fried, S. D.; Bagchi, S.; Boxer, S. G. Measuring Electrostatic Fields in Both Hydrogen Bonding and Non-Hydrogen Bonding Environments Using Carbonyl Vibrational Probes. *J. Am. Chem. Soc.* **2013**, *135*, 11181–11192.
(16) Kozuch, J.; Schneider, S.; Zheng, C.; et al. Testing the Limitations of MD-Based Local Electric Fields Using the Vibrational Stark Effect in Solution: Penicillin G as a Test Case. *J. Phys. Chem. B* **2021**, *125*, 4415–4427.
(17) Levinson, N. M.; Fried, S. D.; Boxer, S. G. Solvent-Induced Infrared Frequency Shifts in Aromatic Nitriles Are Quantitatively Described by the Vibrational Stark Effect. *J. Phys. Chem. B* **2012**, *116*, 10470–10476.
(18) Biava, H.; Schreiber, T.; Katz, S.; et al. Long-Range Modulations of Electric Fields in Proteins. *J. Phys. Chem. B* **2018**, *122*, 8330–8342.
(19) Staffa, J. K. J. K.; Lorenz, L.; Stolarski, M.; et al. Determination of the Local Electric Field at Au/SAM Interfaces Using the Vibrational Stark Effect. *J. Phys. Chem. C* **2017**, *121*, 22274–22285.
(20) Patrow, J. G.; Sorenson, S. A.; Dawlaty, J. M. Direct Spectroscopic Measurement of Interfacial Electric Fields near an Electrode under Polarizing or Current-Carrying Conditions. *J. Phys. Chem. C* **2017**, *121*, 11585–11592.
(21) Wright, D.; Sangtarash, S.; Mueller, N. S.; et al. Vibrational Stark Effects: Ionic Influence on Local Fields. *J. Phys. Chem. Lett.* **2022**, *13*, 4905–4911.
(22) Shi, H.; Pekarek, R. T.; Chen, R.; et al. Monitoring Local Electric Fields Using Stark Shifts on Napthyl Nitrile-Functionalized Silicon Photoelectrodes. *J. Phys. Chem. C* **2020**, *124*, 17000–17005.
(23) Hu, W.; Webb, L. J. Direct Measurement of the Membrane Dipole Field in Bicelles Using Vibrational Stark Effect Spectroscopy. *J. Phys. Chem. Lett.* **2011**, *2*, 1925–1930.
(24) Shrestha, R.; Cardenas, A. E.; Elber, R.; Webb, L. J. Measurement of the Membrane Dipole Electric Field in DMPC Vesicles Using Vibrational Shifts of P-Cyanophenylalanine and Molecular Dynamics Simulations. *J. Phys. Chem. B* **2015**, *119*, 2869–2876.
(25) Utesch, T.; Staffa, J.; Katz, S.; et al. Potential Distribution across Model Membranes. *J. Phys. Chem. B* **2022**, *126*, 7664–7675.
(26) Fried, S. D.; Bagchi, S.; Boxer, S. G. Extreme Electric Fields Power Catalysis in the Active Site of Ketosteroid Isomerase. *Science* **2014**, *346*, 1510–1514.
(27) Schneider, S. H.; Kozuch, J.; Boxer, S. G. The Interplay of Electrostatics and Chemical Positioning in the Evolution of Antibiotic Resistance in TEM β-Lactamases. *ACS Centr. Sci.* **2021**, *7*, 1996–2008.
(28) Baserga, F.; Dragelj, J.; Kozuch, J.; et al. Quantification of Local Electric Field Changes at the Active Site of Cytochrome c Oxidase by Fourier Transform Infrared Spectroelectrochemical

Titrations. *Front. Chem.* **2021**, *9*, 1–13.
(29) Ji, Z.; Kozuch, J.; Mathews, I. I.; et al. Protein Electric Fields Enable Faster and Longer-Lasting Covalent Inhibition of β-Lactamases. *J. Am. Chem. Soc.* **2022**, *144*, 20947–20954.
(30) Ramos, S.; Horness, R. E.; Collins, J. A.; et al. Site-Specific 2D IR Spectroscopy: A General Approach for the Characterization of Protein Dynamics with High Spatial and Temporal Resolution. *Phys. Chem. Chem. Phys.* **2019**, *21*, 780–788.
(31) Baiz, C. R.; Błasiak, B.; Bredenbeck, J.; et al. Vibrational Spectroscopic Map, Vibrational Spectroscopy, and Intermolecular Interaction. *Chem. Rev.* **2020**, *120*, 7152–7218.
(32) Zheng, C.; Mao, Y.; Kozuch, J.; et al. A Two-Directional Vibrational Probe Reveals Different Electric Field Orientations in Solution and an Enzyme Active Site. *Nat. Chem.* **2022**, *14*, 891–897.
(33) Pazos, I. M.; Ghosh, A.; Tucker, M. J.; Gai, F. Ester Carbonyl Vibration as a Sensitive Probe of Protein Local Electric Field. *Angew. Chemie Int. Ed.* **2014**, *53*, 6080–6084.
(34) Lee, H.; Choi, J. H.; Cho, M. Vibrational Solvatochromism and Electrochromism. II. Multipole Analysis. *J. Chem. Phys.* **2012**, *137*, 114307.
(35) Fried, S. D.; Wang, L.-P. P.; Boxer, S. G.; et al. Calculations of the Electric Fields in Liquid Solutions. *J. Phys. Chem. B* **2013**, *117*, 16236–16248.
(36) Schneider, S. H.; Boxer, S. G. Vibrational Stark Effects of Carbonyl Probes Applied to Reinterpret IR and Raman Data for Enzyme Inhibitors in Terms of Electric Fields at the Active Site. *J. Phys. Chem. B* **2016**, *120*, 9672–9684.
(37) Suydam, I. T.; Snow, C. D.; Pande, V. S.; Boxer, S. G. Electric Fields at the Active Site of an Enzyme: Direct Comparison of Experiment with Theory. *Science* **2006**, *313*, 200–204.
(38) Błasiak, B.; Ritchie, A. W.; Webb, L. J.; Cho, M. Vibrational Solvatochromism of Nitrile Infrared Probes: Beyond the Vibrational Stark Dipole Approach. *Phys. Chem. Chem. Phys.* **2016**, *18*, 18094–18111.
(39) Adhikary, R.; Zimmermann, J.; Romesberg, F. E. Transparent Window Vibrational Probes for the Characterization of Proteins with High Structural and Temporal Resolution. *Chem. Rev.* **2017**, *117*, 1927–1969.
(40) Kraskov, A.; Von Sass, J.; Nguyen, A. D.; et al. Local Electric Field Changes during the Photoconversion of the Bathy Phytochrome Agp2. *Biochemistry* **2021**, *60*, 2967–2977.
(41) Shirley, J. C.; Baiz, C. R. Experimental Two-Dimensional Infrared Spectra of Methyl Thiocyanate in Water and Organic Solvents. *J. Chem. Phys.* **2024**, *160*, 114501.
(42) Van Wilderen, L. J. G. W.; Kern-Michler, D.; Müller-Werkmeister, H. M.; Bredenbeck, J. Vibrational Dynamics and Solvatochromism of the Label SCN in Various Solvents and Hemoglobin by Time Dependent IR and 2D-IR Spectroscopy. *Phys. Chem. Chem. Phys.* **2014**, *16*, 19643–19653.
(43) Xu, R. J.; Blasiak, B.; Cho, M.; et al. A Direct, Quantitative Connection between Molecular Dynamics Simulations and Vibrational Probe Line Shapes. **2018**, *9*.
(44) Gasse, P.; Stensitzki, T.; Mai-Linde, Y.; et al. 2D-IR Spectroscopy of Carbohydrates: Characterization of Thiocyanate-Labeled β -Glucose in CHCl3and H2O. *J. Chem. Phys.* **2023**, *158*, 145101.
(45) Völler, J.-S.; Biava, H.; Hildebrandt, P.; Budisa, N. An Expanded Genetic Code for Probing the Role of Electrostatics in Enzyme Catalysis by Vibrational Stark Spectroscopy. *Biochim. Biophys. Acta* **2017**, *1861*, 3053–3059.
(46) Fleming, F. F.; Yao, L.; Ravikumar, P. C.; et al. Nitrile-Containing Pharmaceuticals: Efficacious Roles of the Nitrile Pharmacophore. *J. Med. Chem.* **2010**, *53*, 7902–7917.
(47) Schkolnik, G.; Salewski, J.; Millo, D.; et al. Vibrational Stark Effect of the Electric-Field Reporter 4-Mercaptobenzonitrile as a Tool for Investigating Electrostatics at Electrode/SAM/Solution Interfaces. *Int. J. Mol. Sci.* **2012**, *13*, 7466–7482.
(48) Fafarman, A. T.; Sigala, P. A.; Herschlag, D.; Boxer, S. G. Decomposition of Vibrational Shifts of Nitriles into Electrostatic and Hydrogen-Bonding Effects. *J. Am. Chem. Soc.* **2010**, *132*, 12811–12813.
(49) Choi, J. H.; Oh, K. I.; Lee, H.; et al. Nitrile and Thiocyanate IR Probes: Quantum Chemistry Calculation Studies and Multivariate Least-Square Fitting Analysis. *J. Chem. Phys.* **2008**, *128*, 134506.
(50) Weaver, J. B.; Kozuch, J.; Kirsh, J. M.; Boxer, S. G. Nitrile Infrared Intensities Characterize Electric Fields and Hydrogen Bonding in Protic, Aprotic, and Protein Environments. *J. Am. Chem. Soc.* **2022**, *144*, 7562–7567.
(51) Suydam, I. T.; Boxer, S. G. Vibrational Stark Effects Calibrate the Sensitivity of Vibrational Probes for Electric Fields in Proteins. *Biochemistry* **2003**, *42*, 12050–12055.
(52) Kirsh, J. M.; Weaver, J. B.; Boxer, S. G.; Kozuch, J. Critical Evaluation of Polarizable and Nonpolarizable Force Fields for Proteins Using Experimentally Derived Nitrile Electric Fields. *J. Am. Chem. Soc.* **2024**, *146*, 6983–6991.
(53) Deb, P.; Haldar, T.; Kashid, S. M.; et al. Correlating Nitrile IR Frequencies to Local Electrostatics Quantifies Noncovalent Interactions of Peptides and Proteins. *J. Phys. Chem. B* **2016**, *120*, 4034–4046.
(54) First, J. T.; Slocum, J. D.; Webb, L. J. Quantifying the Effects of Hydrogen Bonding on Nitrile Frequencies in GFP: Beyond Solvent Exposure. *J. Phys. Chem. B* **2018**, *122*, 6733–6743.
(55) Chen, M.; Ko, H. Y.; Remsing, R. C.; et al. Ab Initio Theory and Modeling of Water. *Proc. Natl. Acad. Sci. U. S. A.* **2017**, *114*, 10846–10851.
(56) Andersson, M. P.; Uvdal, P. New Scale Factors for Harmonic Vibrational Frequencies Using the B3LYP Density Functional Method with the Triple-ζ Basis Set 6-311+G(d,P). *J. Phys. Chem. A* **2005**, *109*, 2937–2941.
(57) Ren, P.; Wu, C.; Ponder, J. W. Polarizable Atomic Multipole-Based Molecular Mechanics for Organic Molecules. *J. Chem. Theory Comput.* **2011**, *7*, 3143–3161.
(58) Lin, Y. C.; Ren, P.; Webb, L. J. AMOEBA Force Field Trajectories Improve Predictions of Accurate p KaValues of the GFP Fluorophore: The Importance of Polarizability and Water Interactions. *J. Phys. Chem. B* **2022**, *126*, 7806–7817.
(59) Barth, E.; Kuczera, K.; Leimkuhler, B.; Skeel, R. D. Algorithms for Constrained Molecular Dynamics. *J. Comput. Chem.* **1995**, *16*, 1192–1209.
(60) Weingerl, U.; Fischer, J. Consideration of Dipole–Quadrupole Interactions in Molecular Based Equations of State. *Fluid Phase Equilib.* **2002**, *202*, 49–66.
(61) Buckingham, R. A. The Classical Equation of State of Gaseous Helium, Neon and Argon. *Proc. R. Soc. London. Ser. A. Math. Phys. Sci.* **1938**, *168*, 264–283.
(62) Surulere, S. A.; Shatalov, M. Y.; Olayiwola, F. E. Extensive Study of Modern Approaches Used in Identifying the Buckingham Potential. *Int. J. Appl. Comput. Math.* **2024**, *10*, 1–19.
(63) Karssemeijer, L. J.; Pedersen, A.; Jónsson, H.; Cuppen, H. M. Long-Timescale Simulations of Diffusion in Molecular Solids. *Phys. Chem. Chem. Phys.* **2012**, *14*, 10844–10852.
(64) Mukherjee, S.; Ji, Z.; Andreo, J.; et al. Electrostatic Atlas of Noncovalent Interactions Built in Metal-Organic Frameworks. *ChemRxiv* **2024**.
(65) Auer, B. M.; Skinner, J. L. Dynamical Effects in Line Shapes for Coupled Chromophores: Time-Averaging Approximation. *J. Chem. Phys.* **2007**, *127*, 104105.
(66) Kleckner, I. R.; Foster, M. P. An Introduction to NMR-Based Approaches for Measuring Protein Dynamics. *Biochim. Biophys. Acta - Proteins Proteomics* **2011**, *1814*, 942–968.
(67) Schmidt, J. R.; Corcelli, S. A. Infrared Absorption Line Shapes in the Classical Limit: A Comparison of the Classical Dipole and Fluctuating Frequency Approximations. *J. Chem. Phys.* **2008**, *128*.
(68) Layfield, J. P.; Hammes-Schiffer, S. Calculation of Vibrational Shifts of Nitrile Probes in the Active Site of Ketosteroid Isomerase upon Ligand Binding. *J. Am. Chem. Soc.* **2013**, *135*, 717–725.
(69) Bagchi, S.; Boxer, S. G.; Fayer, M. D. Ribonuclease S Dynamics Measured Using a Nitrile Label with 2D IR Vibrational Echo Spectroscopy. *J. Phys. Chem. B* **2012**, *116*, 4034–4042.
(70) Błasiak, B.; Londergan, C. H.; Webb, L. J.; Cho, M. Vibrational Probes: From Small Molecule Solvatochromism Theory and Experiments to Applications in Complex Systems. *Acc. Chem. Res.* **2017**, *50*, 968–976.
(71) Li, X. Z.; Walker, B.; Michaelides, A. Quantum Nature of the Hydrogen Bond. **2011**, *108*.
(72) Grabowski, S. J. What Is the Covalency of Hydrogen Bonding? *Chem. Rev.* **2011**, *111*, 2597–2625.
(73) Shaik, S.; Danovich, D.; Zare, R. N. Valence Bond Theory Allows a Generalized Description of Hydrogen Bonding. *J. Am. Chem. Soc.* **2023**, *145*, 20132–20140.

(74) Xiong, H.; Lee, J. K.; Zare, R. N.; Min, W. Strong Electric Field Observed at the Interface of Aqueous Microdroplets. *J. Phys. Chem. Lett.* **2020**, *11*, 7423–7428.
(75) Lee, C.; Yang, W.; Parr, R. G. Development of the Colic-Salvetti Correlation-Energy into a Functional of the Electron Density Formula. *Phys. Rev. B* **1988**, *37*, 785–789.
(76) Stephen, P. J.; Devlin, F. J.; Chabalowski, C. F.; Frisch, M. J. Ab Initio Calculation of Vibrational Absorption. *J. Phys. Chem.* **1994**, *98*, 11623–11627.
(77) Caldeweyher, E.; Bannwarth, C.; Grimme, S. Extension of the D3 Dispersion Coefficient Model. *J. Chem. Phys.* **2017**, *147*, 034112.
(78) McLean, A. D.; Chandler, G. S. Contracted Gaussian Basis Sets for Molecular Calculations. I. Second Row Atoms, Z=11-18. *J. Chem. Phys.* **1980**, *72*, 5639–5648.
(79) Krishnan, R.; Binkley, J. S.; Seeger, R.; Pople, J. A. Self - Consistent Molecular Orbital Methods. XX. A Basis Set for Correlated Wave Functions. *J. Chem. Phys* **1980**, *72*, 650–654.
(80) Chubb, K. L.; Tennyson, J.; Yurchenko, S. N. ExoMol Molecular Line Lists – XXXVII. Spectra of Acetylene. *Mon. Not. R. Astron. Soc.* **2020**, *493*, 1531–1545.
(81) Schnieders, M. J.; Rackers, J. A.; Wang, Z.; et al. Tinker8: Software Tools for Molecular Design. *J. Chem. Theory Comput.* **2018**, *14*, 5273–5289.
(82) Shi, Y.; Xia, Z.; Zhang, J.; et al. Polarizable Atomic Multipole-Based AMOEBA Force Field for Proteins. *J. Chem. Theory Comput.* **2013**, *9*, 4046–4063.
(83) Wang, Z.; Ponder, J. W. Tinker9: Next Generation of Tinker with GPU Support https://github.com/TinkerTools/tinker9.
(84) Walker, B.; Liu, C.; Wait, E.; Ren, P. Automation of AMOEBA Polarizable Force Field for Small Molecules: Poltype 2. *J. Comput. Chem.* **2022**, *43*, 1530–1542.
(85) Dalosto, S. D.; Vanderkooi, J. M.; Sharp, K. A. Vibrational Stark Effects on Carbonyl, Nitrile, and Nitrosyl Compounds Including Heme Ligands, CO, CN, and NO, Studied with Density Functional Theory. *J. Phys. Chem. B* **2004**, *108*, 6450–6457.
(86) Cruz, R.; Ataka, K.; Heberle, J.; Kozuch, J. Evaluating Aliphatic CF, CF2 and CF3 Groups as Vibrational Stark Effect Reporters. *J. Chem. Phys* **2024**, *160*, 204308.
(87) Frisch, M. J.; Trucks, G. W.; Schlegel, H. B.; et al. Gaussian 16. Gaussian, Inc.,: Wallingford CT 2016.
(88) Becke, A. D. Density-functional Thermochemistry. III. The Role of Exact Exchange. *J. Chem. Phys.* **1993**, *98*, 5648–5652.